ISSN 0915-633X

NATIONAL INSTITUTE FOR FUSION SCIENCE

Impulsive Alfven Coupling between the Magnetosphere and Ionosphere

R. V. Reddy, K. Watanabe, T. Sato and T. H. Watanabe

(Received – Mar. 22, 1994)

NIFS-276 Apr. 1994

RESEARCH REPORT
NIFS Series

NAGOYA, JAPAN

Impulsive Alfven Coupling between the Magnetosphere and Ionosphere

R. V. Reddy [1)], K. Watanabe, T. Sato, and T. H. Watanabe

National Institute for Fusion Science, Nagoya 464-01, Japan

Abstract

Basic properties of the impulsive Alfven interaction between the magnetosphere and ionosphere have been studied by means of a three-dimensional self-consistent simulation of the coupled magnetosphere and ionosphere system. It is found that the duration time of an impulsive perturbation at the magnetospheric equator, the latitudinal distribution of the Alfven propagation time along the field lines, and the ratio between the magnetospheric impedance and the ionospheric resistance is the main key factors that determine the propagation dynamics and the ionospheric responses for an impulsive MHD perturbation in the magnetosphere.

Keywords

magnetosphere-ionosphere coupling, Alfven wave, geomagnetic pulsation, magnetohydrodynamics, MHD simulation

1) Permanent address : *Indian Institute of Geomagnetism, Colaba, Bombay 400005, India*

§ 1 Introduction

The magnetic pulsating phenomena observed on the earth, called the geomagnetic pulsation, have long been studied by many authors. It is said that the pulsating behavior of the geomagnetic field, especially, the irregular pulsation (Pi), is caused by the MHD waves which are excited in the magnetosphere and propagate along the field lines between the magnetosphere and ionosphere [1-4]. In spite of the tremendous data accumulation of geomagnetic pulsations which are made on the ground or by the spacecraft, the causal mechanism has not yet been fully clarified. Because of the smallness of the signal/noise ratio, it is unbelievably difficult to observe an MHD signal by spacecraft near the plasma sheet at which its origin would be born. Therefore, the relationship between the magnetic pulsating signal observed on the ground and the original signal born in the magnetosphere, namely, the cause and effect relationship of the pulsation is hard to be made clear.

In order to deepen our understanding of the geomagnetic pulsation phenomena such as Pi 2, we focus merely on the basic properties of an impulsive Alfven wave interaction between the magnetosphere and ionosphere. We rely on a three-dimensional simulation model where the magnetohydrodynamic (MHD) equations are solved for the magnetosphere and the height-integrated ionospheric equations for the ionosphere, based on Sato's theory [5]. The ionosphere, therefore, is not a simple reflector of the wave which propagates from the magnetosphere, but, a more realistic magnetosphere-ionosphere interaction including the ohmic dissipation in the ionosphere is dealt with self-consistently.

A high conductivity case corresponding to the day-side ionosphere and a low conductivity case corresponding to the night-side ionosphere are considered independently. The duration time of an impulsive perturbation imposed upon the magnetospheric equator is varied with intent to study the difference in the dynamic response pattern of the perturbation. Also studied is the difference in the dynamic response depending on whether

the Alfven propagation time between the magnetosphere and ionosphere is latitudinally uniform or non-uniform.

The simulation model and the simulation results are discussed in section 2 and 3, respectively. In section 4, summary and discussion are given.

§ 2 Simulation Model and Procedure

2.1 Basic Equations

We adopt one-fluid MHD equations to represent the fully ionized and collisionless magnetospheric plasma. The basic set of equations are given by

$$\frac{\partial \boldsymbol{B}}{\partial t} = -\nabla \times \boldsymbol{E}, \tag{1}$$

$$\frac{\partial \boldsymbol{v}}{\partial t} + (\boldsymbol{v}\cdot\nabla)\boldsymbol{v} = \frac{1}{\rho_0}(\boldsymbol{j} \times \boldsymbol{B}), \tag{2}$$

$$\boldsymbol{E} = -\boldsymbol{v} \times \boldsymbol{B}, \tag{3}$$

$$\mu_0 \boldsymbol{j} = \nabla \times \boldsymbol{B}, \tag{4}$$

where $\boldsymbol{B}$, $\boldsymbol{v}$, $\boldsymbol{E}$, and $\boldsymbol{j}$ are the magnetic field, the velocity of the plasma flow, the electric field and the current density, respectively; ρ_0 and μ_0 are the plasma mass density and permeability. We assume the plasma mass density and plasma temperature to be constant in time and discard the contribution of compressional modes.

To represent the ionosphere where the plasma is weakly ionized, we employ a current continuity equation between the height integrated ionospheric current and the field-aligned current through the magnetosphere [5], namely, the ionospheric equation is given by

$$\nabla_\perp \cdot \boldsymbol{I}_I = -j_I, \tag{5}$$

where j_I is the field-aligned current density at the ionospheric height and $\boldsymbol{I}_I$ is the height integrated ionospheric current. The height integrated ionospheric current is given by

$$\boldsymbol{I}_I = ehM_P N \boldsymbol{E}_I - ehM_H N \frac{\boldsymbol{E}_I \times \boldsymbol{B}_I}{|\boldsymbol{B}_I|}, \tag{6}$$

where $\boldsymbol{E}_I$, N and $\boldsymbol{B}_I$ are the height-averaged ionospheric electric field, the height-averaged number density and the height-averaged ionospheric magnetic field, respectively; e, h, M_P, and M_H are the electric charge, the effective height of the ionosphere, the Pedersen mobility and the Hall mobility, respectively. Thus, the first and second terms in Eq. (6) represent the Pedersen and Hall currents, respectively.

Since the ionosphere is a highly resistive medium, we can assume that $\boldsymbol{E}_I$ is the electrostatic field which can be expressed as $\boldsymbol{E}_I = -\nabla\Phi$, where Φ is an electrostatic potential. Substitution of Eq. (6) into Eq. (5) using the electrostatic potential yields an elliptic-like equation with the variable coefficients,

$$\nabla_\perp \cdot [ehM_P N\nabla\Phi - ehM_H N\frac{\nabla\Phi \times \boldsymbol{B}_I}{\mid \boldsymbol{B}_I \mid}] = j_I. \tag{7}$$

The wave propagation in the magnetosphere-ionosphere coupling system is investigated by solving the equations (1)-(7) simultaneously.

2.2 Numerical Model and Boundary Conditions

The numerical model is similar to the model presented by Watanabe et al. [6-8] . The model and the boundary conditions are briefly summarized here. A spherical coordinate system (r, θ, ϕ) is used to represent the simulation model, where the center of the earth is located at $r = 0$; the north pole and the midnight meridian plane correspond to $\theta = 0$ and $\phi = 0$, respectively. The ionosphere corresponds to the spherical plane at $r = 1R_E$ and the magnetospheric equatorial plane correspond to that at $r = 10R_E$. We employ a radially straight magnetic field line model, $\boldsymbol{B}_0 = B_I(R_E/r)^2\boldsymbol{r}$, ($B_I = -3.1 \times 10^{-5}$ Tesla ; the geomagnetic intensity at the ionospheric height) of which divergence is equal to be 0. Thus, the ionosphere is coupled with the magnetosphere through the magnetic field line. At the ionospheric boundary, the electric field is given through Eq.(7), where the electric field, $\boldsymbol{E}$, is obtained from $-\nabla\Phi$. The high and low latitudinal boundaries are located at

80° and 60° latitudes, respectively, i.e., $\theta = 10\pi/180$ and $\theta = 30\pi/180$. At the latitudinal boundaries we assume the fixed boundary condition both for the plasma velocity and the magnetic field. The longitudinal coordinate ϕ is taken in the anticlockwise direction (see Fig.2 in Watanabe et al. [6]). In the longitudinal direction we employ the periodic boundary condition.

In the magnetospheric equatorial boundary ($r = 10R_E$), we impose a localized convection flow both in space and time as a driving source for the excitation of an impulsive signal. Then, the localized convection flow excites an Alfven perturbation which propagates through the magnetosphere towards the ionosphere along the field lines. When the Alfven perturbation arrives at the ionosphere, the field-aligned current accompanied with the Alfven perturbation excites an ionospheric electric field, hence, an ionospheric current, through Eq.(7). The ionospheric electric field reflects back to the magnetospheric equator. The reflection rate is determined by the ratio of the ionospheric resistance to the magnetospheric characteristic impedance.

In this paper we consider the Alfven wave coupling on the day side and on the night side as separate cases. The density is taken to be constant along the longitudinal direction, since the geomagnetic pulsation phenomena are highly localized in the longitude in the ionosphere. For the night-side case we have given the typical height-averaged ionospheric density as $N = 1.0 \times 10^{10}/\mathrm{m}^3$, and for the day-side case as $N = 1.0 \times 10^{11}/\mathrm{m}^3$.

First, in order to clarify the simple Alfven coupling between the magnetosphere and ionosphere, we chose the Alfven speed to be constant i.e., 1000 km/sec everywhere in the simulation model. Therefore, the Alfven propagation time, $\tau_{A0} = 57.33$ sec, is the same everywhere. In the realistic magnetosphere, however, the Alfven propagation time differs from low latitude to the high latitude ionosphere, namely, the Alfven propagation time at the low latitude is smaller than that at the high latitude, because the length of the field line starting from the low latitude ionosphere to the magnetospheric equator is shorter

than that of the field line from the high latitude ionosphere to the magnetospheric equator. Then, we execute a simulation run in which we chose the Alfven speed distribution in such a way that it varies in the latitudinal direction.

Three cases of the duration time of the initial spatially localized perturbation of convection flow given at the magnetospheric equator, namely, $1/3\tau_{A0}$, $1\tau_{A0}$ and $2.5\tau_{A0}$ are considered to study the dynamic characteristics of Alfven wave coupling. The perturbation of the magnetospheric flow is switched on at time, $t = 0$ and switched off at $t = 1/3\tau_{A0}$, $t = 1\tau_{A0}$ and $2.5\tau_{A0}$, respectively.

We now discuss the simulation procedure. We employ 811 $\times$ 56 $\times$ 38 mesh points in (r, θ, ϕ) coordinates in our simulation box. The basic equations are accordingly transformed into the finite difference equations. The time integration of the MHD equations (1)-(4) is carried out by using the fourth order Runge-Kutta-Gill (RKG) procedure. To solve the elliptic equation, Eq. (7), we adopt the Bi-conjugate gradient method.

Initially, we give the geomagnetic field configuration and the magnetospheric plasma density distribution and set all other variables to be zero. Then, we give a localized convection flow in the magnetospheric equatorial plane at $r = 10R_E$ as an initial condition. We proceed to the main simulation by solving the MHD equations (1)-(4) and obtain the field-aligned current, j_I, at the ionospheric height. Then, substituting j_I in Eq. (7), we determine the electrostatic potential and thereby the electric field and current distributions in the ionosphere. The new ionospheric electric field is used as the boundary condition for the magnetospheric equations at the ionospheric boundary. Then, we repeat the process to advance the time integration.

§ 3 Simulation Results

We have carried out the simulations under the homogeneous and inhomogeneous Alfven speed distributions in the latitudinal direction. The ionospheric density is taken to

be uniform in the longitudinal direction, namely, $N = 1.0 \times 10^{10}/\mathrm{m}^3$ or $N = 1.0 \times 10^{11}/\mathrm{m}^3$ as representing the day-side or night-side density condition, respectively. The flow pattern which is initially given in the magnetospheric equatorial plane is taken to be a localized single vortex. The stream line structure, which is equivalent to the electrostatic potential structure, and the corresponding field-aligned current profile mapped on the ionosphere are shown in Fig. 1-(a) and 1-(b), respectively. The perturbation is given in the flat-top square form in time with three different duration periods, i.e., $1/3\tau_{A0}$, $1\tau_{A0}$, $2.5\tau_{A0}$. The physical parameters of the ionosphere and magnetosphere are given in Table 1 and are the same through out this work.

3.1 Homogeneous Alfven Coupling

First, in order to clarify the basic properties of impulsive Alfven coupling, we start investigating the case of homogeneous coupling where the Alfven speed is constant everywhere and the Alfven propagation time is the same for every field line. The Alfven speed is chosen as 1000 km/sec, and is constant everywhere. Simulation runs are performed for two cases, Case A and B, where the ionospheric resistance, R, is, respectively, larger and smaller than the magnetospheric (Alfvenic) characteristic impedance, Z_0. The former case (Case A) corresponds to the night-side ionosphere and the latter (Case B) to the day-side ionosphere.

Case A:*(night-side case)*

The ionospheric density distribution is given as $N = 1.0 \times 10^{10}/\mathrm{m}^3$. The time evolutions of the ionospheric electrostatic potential and the field-aligned current are shown in Fig. 2 and Fig. 3, respectively. Here, the perturbation is given in three different duration times, namely, (a) $1/3\tau_{A0}$, (b) $1\tau_{A0}$, and (c) $2.5\tau_{A0}$. The main feature of the

temporal development of the ionospheric electrostatic potential and the field-aligned current is determined by the ratio of the ionospheric resistance, R, to the magnetospheric characteristic impedance, Z_0, where $R = \Sigma_P{}^{-1} = 1/(ehM_PN)$ and $Z_0 = \mu_0 V_A$; V_A is the Alfven speed [6,9] .

In the present night-side case, the ratio, R/Z_0, is equal to 2.59. Then, the mismatching between the ionospheric resistance and the magnetospheric characteristic impedance ($R > Z_0$) exhibits several interesting characteristics. First, as can be seen in Fig. 2, the ionospheric potential overshoots the amplitude of the potential given in the equatorial plane, Φ_0, ($\Phi_0 = 20$ kV), at $t = 1\tau_{A0}$, i.e., at the first arrival of the Alfven perturbation at the ionosphere. The overshooted part of the ionospheric potential is observed to be roughly 40% of the potential given at the equatorial plane.

Simple consideration gives us that the overshooted (reflected) potential, $\triangle\Phi$, is given by

$$\triangle\Phi = \frac{R - Z_0}{R + Z_0}\Phi, \tag{8}$$

where Φ is the potential amplitude incident upon the ionosphere; initially $\Phi = \Phi_0$. Plugging the value of $R/Z_0 = 2.59$ gives $\triangle\Phi/\Phi_0 = 44\%$, which is in agreement with the simulation result.

Secondly, the shape of the induced ionospheric potential is a triangle instead of a square. This is because the ionospheric response is given by the time integration of the square-shape pulse. Thirdly, the polarity of the ionospheric electrostatic potential is changed at each successive arrival of the perturbation at the ionosphere. The change of the polarity of the potential at each arrival is explained as follows. The overshooted part of the electric field perturbation at the ionosphere goes back to the magnetospheric equator, and when it arrives there, a new signal is generated so as to cancel the perturbation coming back from the ionosphere. Namely, the newly generated signal at the equator has the polarity which is opposite to that of the incident perturbation. This opposite

polarity perturbation propagates along the field lines and arrives again at the ionosphere, and the same reflection process is repeated thereafter. Thus, the basic response feature is an alternating, damped pulse train with the period of the Alfven bounce time when the duration time of the original impulse is less than the bounce time.

In addition to these features, very interestingly, in the case of the duration period of $2.5\tau_{A0}$, the electrostatic potential exhibits a shoulder structure, e.g., for the period between $t = 3\tau_{A0}$ and $3.5\tau_{A0}$. The formation of this shoulder structure can be understood in the following way. The first signal of the Alfven perturbation arrives at the ionosphere at $t = 1\tau_{A0}$ and the overshooted part of the electric field perturbation reflects back towards the magnetospheric equator. When the reflected overshooted perturbation arrives at the magnetospheric equator at $t = 2\tau_{A0}$, the magnetospheric equator still keeps the original convection flow perturbation. Therefore, a signal is excited at the equator in such a way that the overshooted electric field perturbation is cancelled, namely, its polarity is reversed. Thus, at $t = 3\tau_{A0}$ when the second signal arrives at the ionosphere, the potential drops its amplitude according to the same reflection rule as the first signal has experienced at the ionosphere.

The perturbation at the magnetospheric equator is quitted at $t = 2.5\tau_{A0}$. Therefore, the period of this shoulder is equal to the difference between the bounce time of the Alfven wave and the duration time of the perturbation. In the present case, therefore, this shoulder continues for $0.5\tau_{A0}$ ($= 2.5\tau_{A0} - 2.0\tau_{A0}$). When the original perturbation is quitted at $t = 2.5\tau_{A0}$ at the magnetospheric equator, the negative perturbation whose amplitude is equivalent to the original one is excited and propagates towards the ionosphere. Thus, the potential amplitude experiences a sharp drop by the same amount as the first potential rise at $t = 1\tau_{A0}$ when the negative perturbation arrives at the ionosphere, i.e., at $t = 3.5\tau_{A0}$, as can be seen in Fig. 2-(c). Thus, the ionospheric responses consist of the superposition of two bouncing Alfven signals, one being a positive stepwise signal excited

at $t = 0$ at the magnetospheric equator and the other being a negative stepwise signal with the same amplitude excited at $t = 2.5\tau_{A0}$ at the equator. The shoulder structure, or the interference phase, appears periodically with the bounce period ($2\tau_{A0}$) after the first interference appears.

The time development of the ionospheric field-aligned current has the similar features of that of the ionospheric electrostatic potential as can be seen in Fig. 3. An important difference, however, is that while the potential amplitude can be larger than the original perturbation, the induced ionospheric current is relatively small. Therefore, the geomagnetic signature must be relatively small when the ionospheric conductivity is low.

The equi-contours of the ionospheric potential and the field-aligned current in the case of the duration time of $1\tau_{A0}$ are plotted in Fig. 4-(a) and 4-(b) at $t = 1.35\tau_{A0}$, i.e. at the time during the first arrival of the perturbation at the ionosphere. The equi-contours of the ionospheric potential correspond to the stream lines which are given in the magnetospheric equatorial plane. As can be seen in Fig. 4-(b), the field-aligned current flows into the ionosphere at the mid-latitudinal region and flows back towards the magnetosphere at both higher and lower latitudinal regions.

Case B:*(day-side case)*

The ionospheric density on the day side is given as $N = 1.0 \times 10^{11}/\mathrm{m}^3$. The time development of the ionospheric electrostatic potential and the field-aligned current are shown in Fig. 5 and Fig. 6, respectively, in the similar manner to the night-side case. In the day-side case, the ratio, R/Z_0, is equal to 0.259. In contrast to the night-side case, it is seen that the ionospheric potential undershoots the given amplitude, Φ_0,(Φ_0 = 20 kV) at the first arrival of the perturbation at the ionosphere. The depletion of the ionospheric potential is observed to be roughly 58% of the initial equivalent potential at the equatorial plane. This undershooting feature is explained by Eq. (8) where $\Delta\Phi < 0$

and $|\Delta\Phi/\Phi_0| = 59\%$, which is in agreement with the simulation result.

In the present high conductivity case, the ionospheric pulses have all the same polarity in contrast to the previous low conductivity case. This is because the undershooted part, which has the opposite polarity to the original perturbation, propagates back to the magnetospheric equator and a new signal, which exactly cancels the undershooted perturbation and hence the same polarity as the original one, is generated at the equator. In the case where the initial perturbation amplitude is maintained during $2.5\tau_{A0}$ in the magnetospheric equatorial plane, the ionospheric responses are represented in terms of the superposition of two stepwise signals, one being a positive stepwise signal excited at $t = 0$ at the magnetospheric equator and the other being a negative stepwise signal excited at $t = 2.5\tau_{A0}$ at the equator. This situation is the same as the night-side case. Note, however, that there are some differences. For example, as is evident on comparing Fig. 3-(c) and Fig. 6-(c), the initial offset current remains in the subsequent pulsating behavior far more prominently for the day side than for the night side. Another feature is the difference in the apparent depletion rate of successive pulses ; in the day-side case the rate is roughly $0.43\tau_{A0}^{-1}$, while in the night-side case it is $0.25\tau_{A0}^{-1}$.

Fig. 7-(a) and 7-(b) show the equi-contours of the ionospheric electrostatic potential and the field-aligned current at t = 1.35 τ_{A0}, respectively. Since the resistance on the day side is smaller than that on the night side, the maximum amplitude of the ionospheric field-aligned current on the day side ($0.47\mu\mathrm{A/m}^2$) is larger than that on the night side ($0.17\mu\mathrm{A/m}^2$), while the maximum amplitude of the ionospheric potential on the day side (7.0 kV) is smaller than that on the night side (26.6 kV) due to the smallness of the ratio between the ionospheric resistance and the magnetospheric impedance. This suggests that the geomagnetic pulsating activity can be more easily observed on the day side than on the night side if the other conditions are the same.

3.2 Inhomogeneous Alfven Coupling

In this section, we show the impulsive Alfven wave propagation in a more realistic configuration. Namely, since the field line starting from the low latitude ionosphere to magnetospheric equator is shorter than that from the high latitude, the Alfven propagation time differs from low latitude to high latitude ionosphere. Therefore, we employ the Alfven speed profile depending on the latitude, so that we can take account of the difference of the Alfven propagation time. We choose the Alfven speed profile in such a way that it varies only in the latitudinal direction, whereas being constant in the radial and longitudinal directions. The dependence of the Alfven speed on the latitude is given by the following equation,

$$V_A = 500 \times [2 - cos(\pi \frac{(\theta - \theta_{min})}{(\theta_{max} - \theta_{min})}) \ ] \ \text{km/sec.} \tag{9}$$

The maximum Alfven speed is given at the lowest latitude (at θ_{max}) and is equal to 1500 km/sec, while the minimum is at the highest latitude (at θ_{min}) and is equal to 500 km/sec. Accordingly, the Alfven propagation times along the field lines starting from the lowest and highest latitudinal boundaries are given $\tau_{AL} = 0.5\tau_{A0}$ and $\tau_{AH} = 1.5\tau_{A0}$, respectively, which can be considered as reasonable values of the realistic magnetosphere. In the present case, we execute a simulation run separately for the day side and for the night side, similarly to the previous homogeneous Alfven coupling case.

Case A:*(night-side case)*

The time evolutions of the ionospheric electrostatic potential and field-aligned current are shown in Fig. 8 and Fig. 9. For the cases of the duration period, $1/3\tau_{A0}$ and $1\tau_{A0}$, it is found that the maximum amplitude of the ionospheric potential at each arrival of the perturbation is smaller than that in the homogeneous Alfven speed case. For example, in the case of the duration period of $1\tau_{A0}$ (b), the maximum amplitude at the second

arrival of the perturbation at the ionosphere is 10.5 kV, while that in the homogeneous Alfven speed case is 11.2 kV. In contrast to the above small duration time cases, when the duration time of the initial perturbation is $2.5\tau_{A0}$, the maximum amplitude of the ionospheric potential at each arrival of the perturbation is almost the same as that of the homogeneous coupling case.

The reason for this fact may be as follows. Since the Alfven perturbation propagating along the lower latitude field line arrives earlier than that along the higher latitude field line and the duration time of the perturbation given in the magnetospheric equatorial plane is small, e.g., $1/3\tau_{A0}$, it never happens that the ionosphere receives the whole spatial structure of the perturbation simultaneously. Namely, it takes only $2/3\tau_{A0}$ for the perturbation to arrive at the lowest latitude ionosphere, while it does $2\tau_{A0}$ at the highest latitude ionosphere. Then, as far as the perturbation given at the magnetospheric equatorial plane does not continue for the period of $(2\tau_{A0} - 2/3\tau_{A0} =)4/3\tau_{A0}$, there is no time that the whole convective flow perturbation is simultaneously reflected upon the ionosphere. Specifically, since part of the perturbation arrives earlier at lower latitudes, the associated field-aligned current perturbation does not necessarily penetrate into the ionosphere by satisfying the zero-sum condition for the upward and downward currents. However, the zero-sum condition must always be satisfied for the incoming and outgoing field-aligned currents, because otherwise charge-neutrality can not be satisfied. In order to satisfy the zero-sum field-aligned current (charge-neutrality) condition, therefore, the same amount of opposite field-aligned current must be generated in the other part of the ionosphere, say, in the higher latitude region of the ionosphere where the perturbation has not yet arrived. This expansion of the perturbation into higher latitude ionosphere acts to weaken the amplitude of the induced ionospheric potential, as is clear by comparing Fig.2 and Fig. 8. This situation is particularly so, when the duration time of the perturbation is smaller than the difference between the earliest and latest arrival times of the perturbation.

In order to verify this assertion, the equi-contour plots of ionospheric potential and the field-aligned current at $t = 1.35\tau_{A0}$ for the case of the duration time of $1\tau_{A0}$ are given in Fig. 10-(a) and 10-(b), respectively. Comparing Fig. 10-(a) with Fig. 4-(a), one can see a clear surplus potential excitation in the higher latitudinal region where the perturbation has not yet arrived. Due to this surplus (opposite polarity) potential excitation for the short duration case, the spatial diffusivity of the ionospheric potential at each arrival of the perturbation becomes larger as the duration time becomes smaller.

The fact that the whole spatial structure of the perturbation given in the magnetosphere can not arrive simultaneously at the ionosphere leads to another interesting aspect. Comparison of Fig. 10-(b) with 4-(b) finds that the field-aligned current profile, especially the high-latitude positive current region where the current flows out to the magnetosphere, is stretched in the longitudinal direction. This stretching amounts to be 30% compared with the homogeneous coupling case shown in Fig. 4-(b). This is because when the field-aligned current accompanied with the perturbation arrives at the lower latitudinal ionosphere, the Pedersen current flows in the ionosphere, creating the region where the field-aligned current can flow back to the magnetosphere according to the ionospheric conductivity condition. This effect leads to the stretching of the positive field-aligned current region, while in the homogeneous coupling case the whole spatial field-aligned current pattern is created at once and the zero-sum of the upward and downward field-aligned perturbations is always satisfied ; thus, such a stretching in longitudinal direction does not occur.

Case B:*(day-side case)*

For the day-side case, the time evolution of the ionospheric electrostatic potential and the field-aligned current are shown in Fig. 11 and Fig. 12, and the equi-contours at $t = 1.35\tau_{A0}$ are in Fig. 13-(a) and 13-(b). The featuring differences between the

homogeneous and inhomogeneous coupling cases are similar to those observed for the night-side case. Namely, there occurs an invasion of the ionospheric potential into the higher latitudinal region, surplus diffusivity of the potential, and stretching of the field-aligned current profile in the longitudinal direction.

§ 4 Summary and Discussion

We have executed three-dimensional self-consistent simulations of the magnetosphere-ionosphere coupling for studying the basic properties of the impulsive Alfven interaction between the magnetosphere and ionosphere.

First, it is found that the basic frequency of the electric (or magnetic) field perturbation observed in the ionosphere is the Alfven bounce time and the fine structure shows a rather complex feature which consists of the superposition of two stepwise perturbations, one being the onset perturbation and the other being the offset perturbation.

Second, the amplitude and polarity of the induced ionospheric electric field at each arrival of the perturbation at the ionosphere are essentially determined by the ratio of the ionospheric resistance to the magnetospheric impedance.

Third, the large dependence of the Alfven propagation time on the latitude is likely to lead to appreciable change of the field-aligned current distribution and the electric field profile in the ionosphere. Namely, there occur a longitudinal stretching of the field-aligned current region and a latitudinal invasion of the electric field at the region where the perturbation does not arrive. These stretching and invasion effects will be observed in the longer field line (higher latitudinal) region at an earlier time of the pulsating behavior. Because of these effects the induced electric field and current become diffusive and obscure. This is particularly so when the duration time of the perturbation is shorter.

The above results indicate that both the duration time of the perturbation in the magnetosphere and the latitudinal difference in the Alfven propagation time play a crucial

role in the magnetic pulsating phenomena observed on the earth (geomagnetic pulsation).

In addition to the latitudinal dependence of the Alfven propagation time, there is another factor, namely, that the day-side magnetosphere is compressed, while the night-side magnetosphere is extremely extended towards the tail by the solar wind. Therefore, the large difference in the length of the field line between the night side and the day side becomes prominent, indicating that the effect of the Alfven propagation time difference on the pulsating phenomena would be more significant in the night-side pulsation phenomena.

The origin of the perturbation in the magnetosphere remains unclarified. It appears that the perturbation on the day side would be strongly related to the solar wind condition and that the perturbation on the night side would be influenced by the night-side reconnection process. This suggests that, in order to fully understand the geomagnetic pulsation problem, one must invoke a global simulation of the solar wind-magnetosphere interaction(for example, Kageyama et al. [10-11]), but this is surely a future problem.

In this work, the compressional mode is discarded. The compressional mode will be really important in the actual pulsation phenomena. A simulation model including the effects of compressional modes is now under consideration.

Acknowledgments

The authors would like to thank Dr. K. Takahashi for providing his valuable information on the geomagnetic pulsations. One of the authors (R.V.R.) would like to thank Prof. R. Horiuchi, Dr. H. Takamaru, Dr. Y. Todo, and Dr. A. Kageyama for their invaluable help. The work of R.V.R. was supported by the Ministry of Science and Technology, Government of India under the BOYSCAST Fellowships scheme 1991-92.

References

1) Takahashi, K. and S. Ohtani, "AMPTE CCE Observation of Pi 2 Pulsations in the Inner Magnetosphere", *Geophys. Res. Lett., 19*, 1447-1450, 1992.

2) Sutcliffe, P. E. and E. Nielsen, "The Ionospheric Signature of Pi 2 Pulsations Observed by STARE", *J. Geophys. Res., 97*, 10621-10636, 1992.

3) Takahashi, K., N. Sato, J. Warnecke, H. Luhr, H. E. Spence, and Y. Tonegawa, "On the Standing Wave Mode of Giant Pulsations", *J. Geophys. Res., 97*, 10717-10732, 1992.

4) Yeoman, T. K. and D. Orr, "Phase and Spectral Power of Mid-latitude Pi 2 Pulsations : Evidence for a Plasmaspheric Cavity Resonance.", *Plannet. Space Sci., 37*, 1367-1383, 1989.

5) Sato, T. "A Theory of Quiet Auroral Arcs", *J. Geophys. Res., 83*, 1042-1048, 1978.

6) Watanabe, K., M. Ashour-Abdalla, and T. Sato, "A Numerical Model of the Magnetosphere-Ionosphere Coupling, Preliminary Results", *J. Geophys. Res., 91*, 6973-6978, 1986.

7) Watanabe, K. and T. Sato, "Self-Excitation of Auroral Arcs in a Three-Dimensionally Coupled Magnetosphere-Ionosphere System", *Geophys. Res. Lett., 15*, 717-720, 1988.

8) Watanabe, T., H. Oya, K. Watanabe, and T. Sato, "Comprehensive Simulation Study on Local and Global Development of Auroral Arcs and Field-Aligned Potentials", *J. Geophys. Res., 98*, 21391-21407, 1993.

9) Sato, T. and T. Iijima, "A Primary Sources of Large-scale Birkeland Currents", *Space Sci. Rev., 24*, 347-366, 1979.

10) Kageyama, A., K. Watanabe and T. Sato, "A Global Simulation of the Magnetosphere with a Long Tail : no IMF", *J. Geophys. Res., 97*, 3929-3943, 1992.

11) Usadi, A., A. Kageyama, K. Watanabe and T. Sato, "A Global Simulation of the

Magnetosphere with a Long Tail : Southward and Northward IMF", *J. Geophys. Res.*, *98*, 7503-7517, 1993.

Table 1 Physical parameters used in simulations

Ionospheric magnetic field B_I	-3.1×10^{-5} Tesla
Pedersen Mobility M_P	$1.6 \times 10^4 \mathrm{m}^2/\mathrm{sec} \cdot \mathrm{V}$
Hall Mobility M_H	$3.2 \times 10^4 \mathrm{m}^2/\mathrm{sec} \cdot \mathrm{V}$
Effective ionospheric height h	12 km
Alfven propagation time τ_{A0}	57.33 sec
Ionospheric number density on the night side N	$1 \times 10^{10}/\mathrm{m}^3$
Ionospheric number density on the day side N	$1 \times 10^{11}/\mathrm{m}^3$

Figure Captions

Fig. 1 (a) The stream line structure and (b) the corresponding field-aligned current profile mapped on the ionosphere.

Fig. 2 The time evolutions of the ionospheric electrostatic potential in the homogeneous night-side coupling for the cases of the duration time of (a) $1/3\tau_{A0}$, (b) $1\tau_{A0}$, and (c) $2.5\tau_{A0}$.

Fig. 3 The time evolutions of the field-aligned current in the homogeneous night-side coupling for the cases of the duration time of (a) $1/3\tau_{A0}$, (b) $1\tau_{A0}$, and (c) $2.5\tau_{A0}$.

Fig. 4 The equi-contours of (a) the ionospheric potential and (b) the field- aligned current at $t = 1.35\tau_{A0}$ in the homogeneous night-side coupling in the case of the duration time of $1\tau_{A0}$.

Fig. 5 The time evolutions of the ionospheric electrostatic potential in the homogeneous day-side coupling for the cases of the duration time of (a) $1/3\tau_{A0}$, (b) $1\tau_{A0}$, and (c) $2.5\tau_{A0}$.

Fig. 6 The time evolutions of the field-aligned current in the homogeneous day-side coupling for the cases of the duration time of (a) $1/3\tau_{A0}$, (b) $1\tau_{A0}$, and (c) $2.5\tau_{A0}$.

Fig. 7 The equi-contours of (a) the ionospheric potential and (b) the field- aligned current at $t = 1.35\tau_{A0}$ in the homogeneous day-side coupling in the case of the duration time of $1\tau_{A0}$.

Fig. 8 The time evolutions of the ionospheric electrostatic potential in the inhomogeneous night-side coupling for the cases of the duration time of (a) $1/3\tau_{A0}$, (b) $1\tau_{A0}$, and (c) $2.5\tau_{A0}$.

Fig. 9 The time evolutions of the field-aligned current in the inhomogeneous night-side coupling for the cases of the duration time of (a) $1/3\tau_{A0}$, (b) $1\tau_{A0}$, and (c) $2.5\tau_{A0}$.

Fig. 10 The equi-contours of (a) the ionospheric potential and (b) the field- aligned current at $t = 1.35\tau_{A0}$ in the inhomogeneous night-side coupling in the case of

the duration time of $1\tau_{A0}$.

Fig. 11 The time evolutions of the ionospheric electrostatic potential in the inhomogeneous day-side coupling for the cases of the duration time of (a) $1/3\tau_{A0}$, (b) $1\tau_{A0}$, and (c) $2.5\tau_{A0}$.

Fig. 12 The time evolutions of the field-aligned current in the inhomogeneous day-side coupling for the cases of the duration time of (a) $1/3\tau_{A0}$, (b) $1\tau_{A0}$, and (c) $2.5\tau_{A0}$.

Fig. 13 The equi-contours of (a) the ionospheric potential and (b) the field- aligned current at $t = 1.35\tau_{A0}$ in the inhomogeneous day-side coupling in the case of the duration time of $1\tau_{A0}$.

(a) Plasma Stream Line

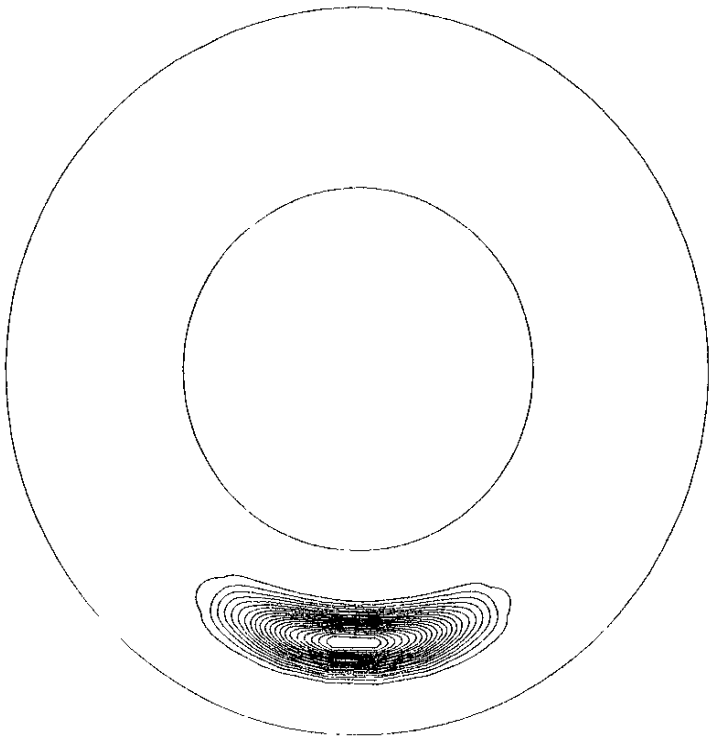

(b) Field-Aligned Current

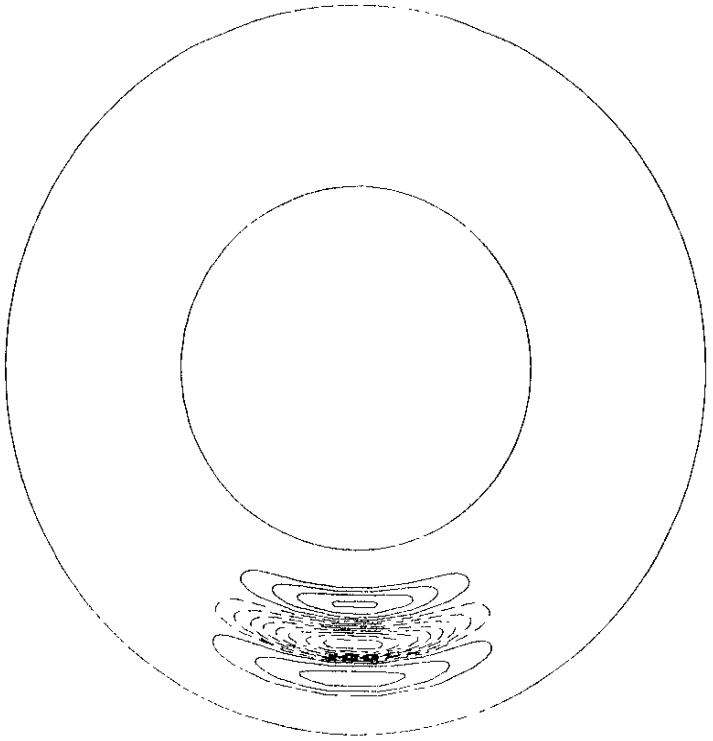

Fig. 1

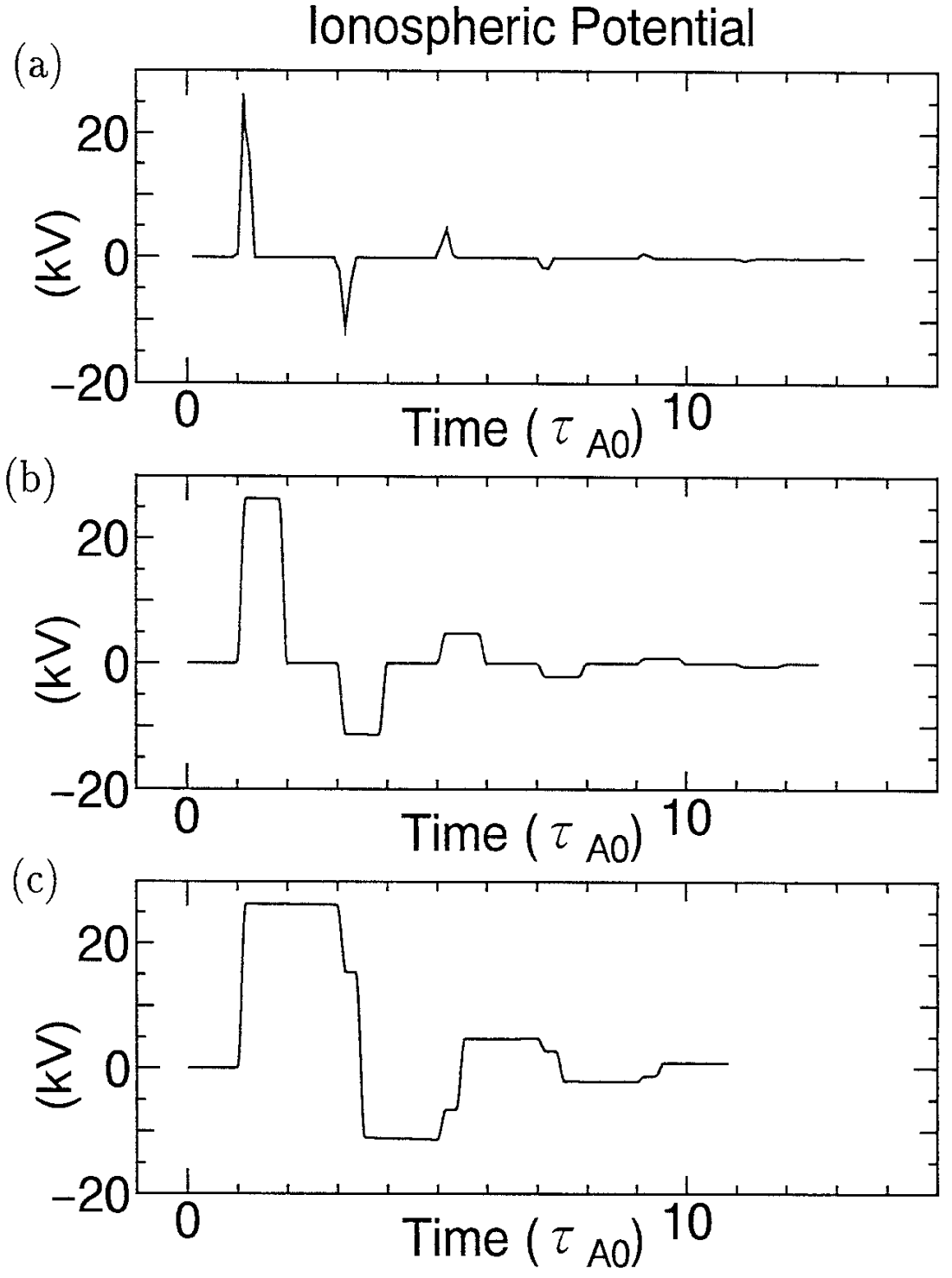
Ionospheric Potential
(a)
20
0
−20
(kV)
0
Time (τ_{A0}) 10
(b)
20
0
−20
(kV)
0
Time (τ_{A0}) 10
(c)
20
0
−20
(kV)
0
Time (τ_{A0}) 10

Fig. 2

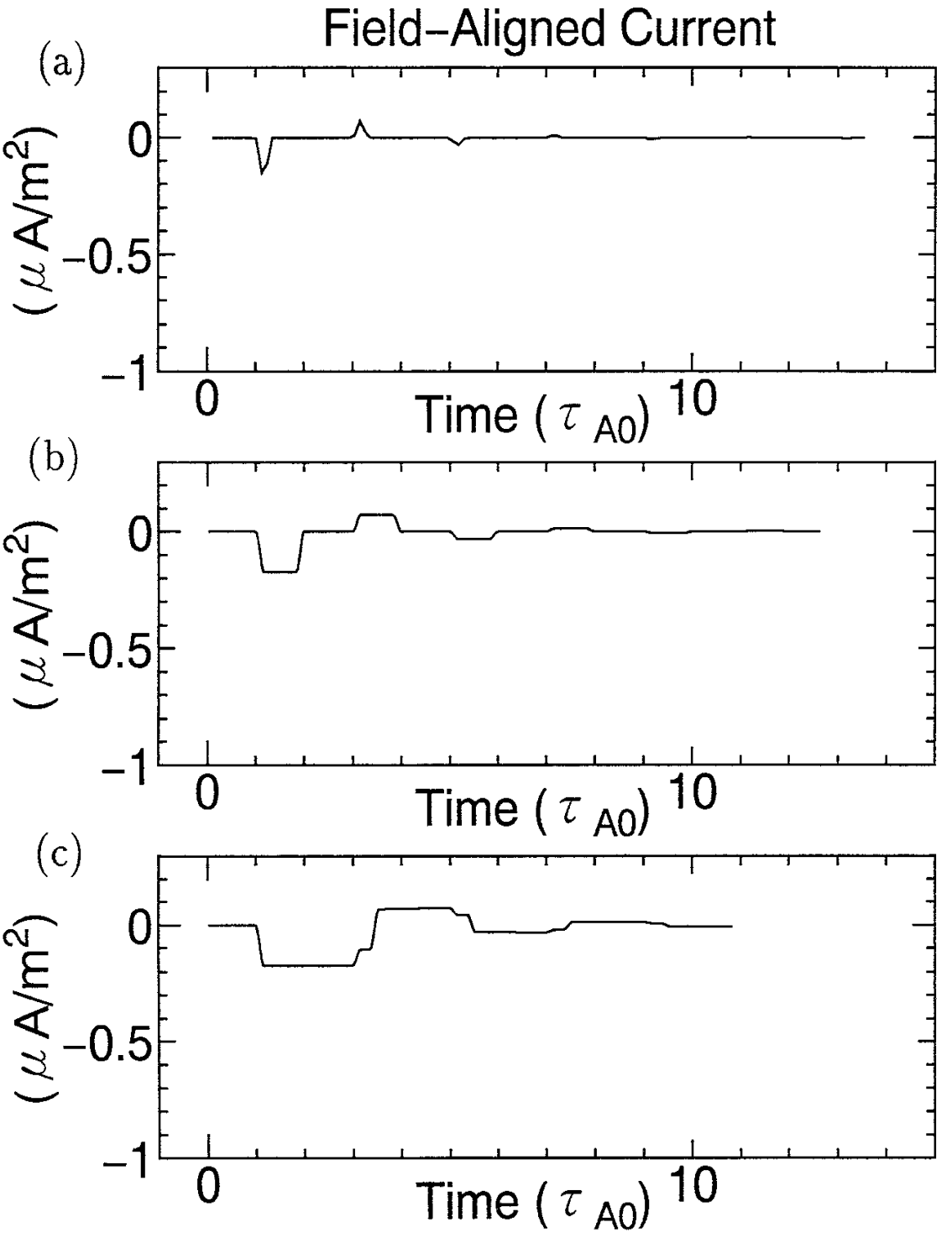

Fig. 3

(a) Electrostatic Potential

(b) Field-Aligned Current

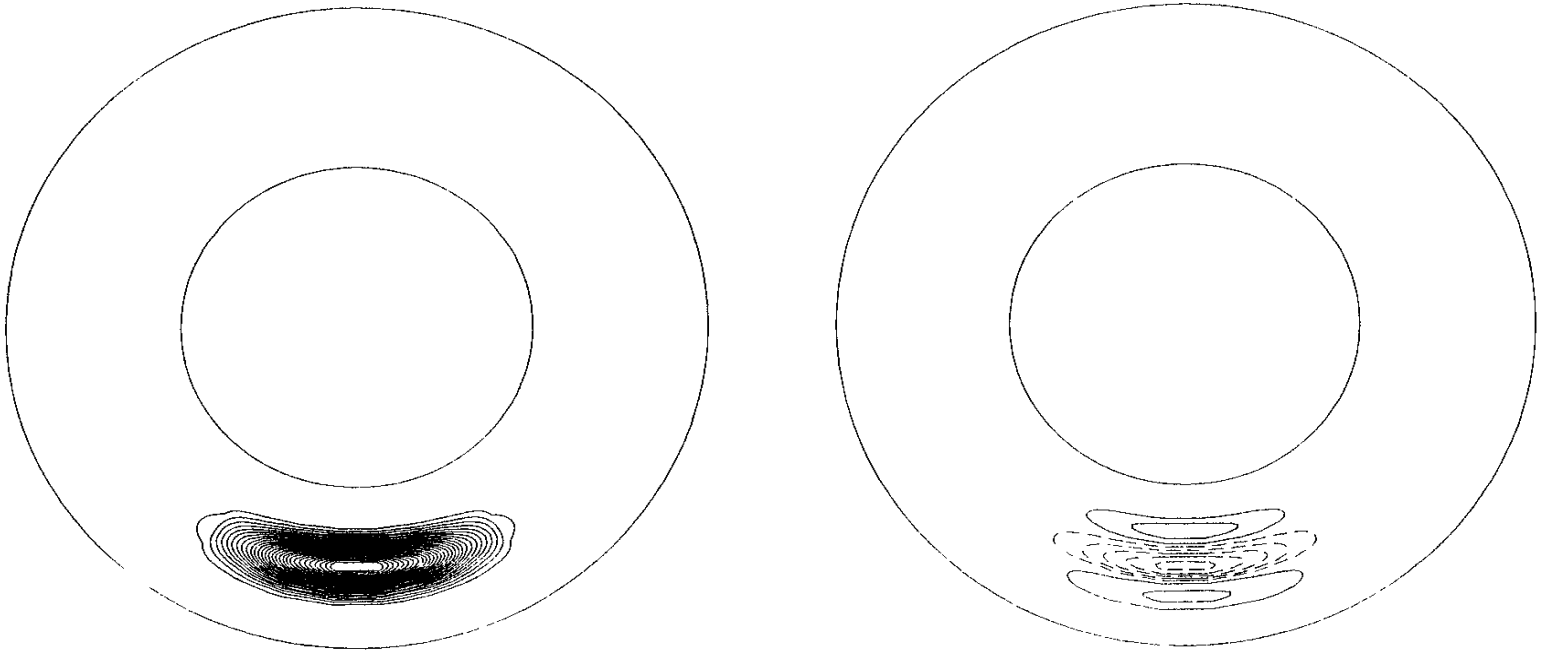

Fig. 4

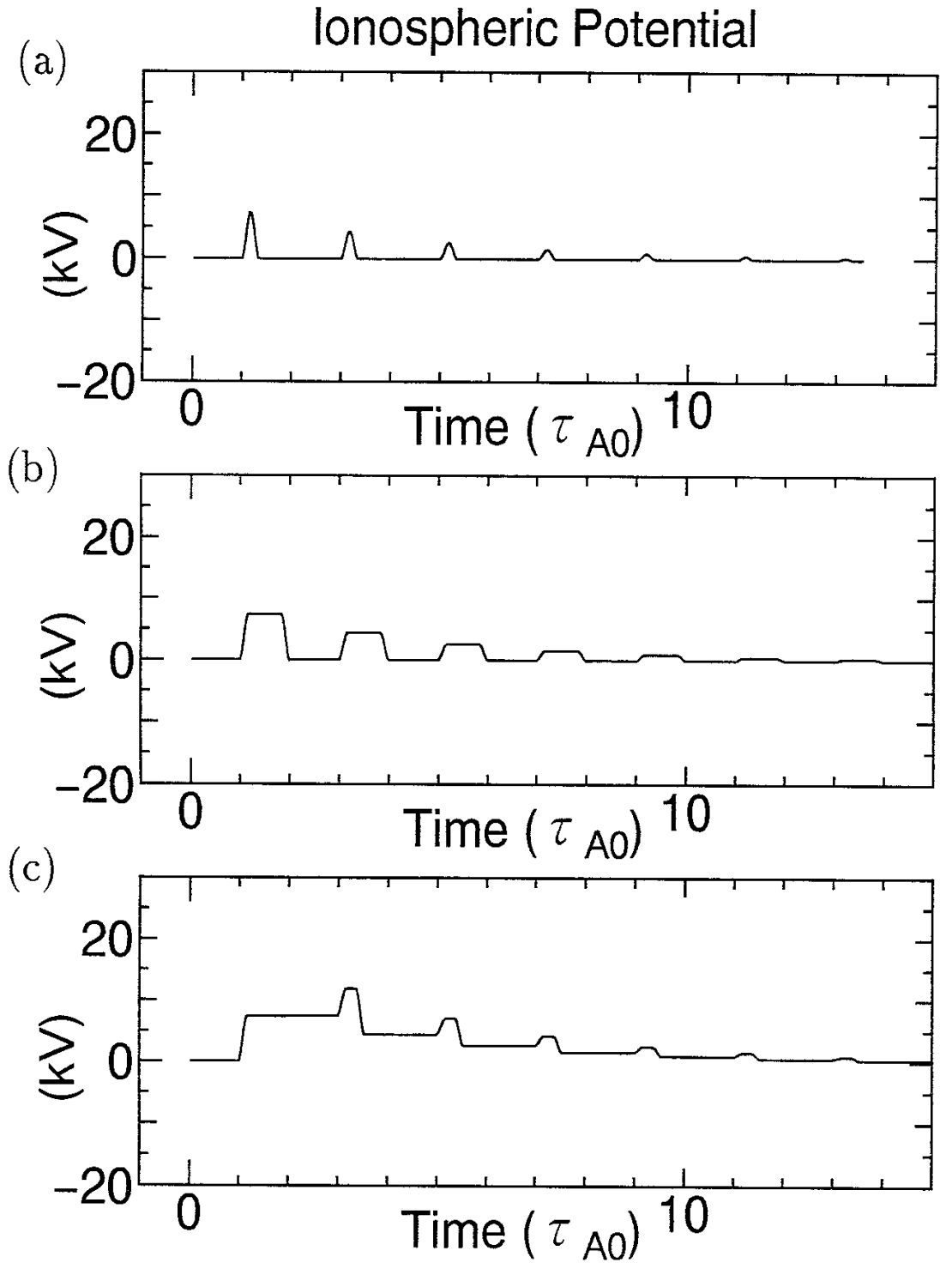
Ionospheric Potential
(a)
20
0
-20
(kV)
0
Time (τ_{A0}) 10
(b)
20
0
-20
(kV)
0
Time (τ_{A0}) 10
(c)
20
0
-20
(kV)
0
Time (τ_{A0}) 10

Fig. 5

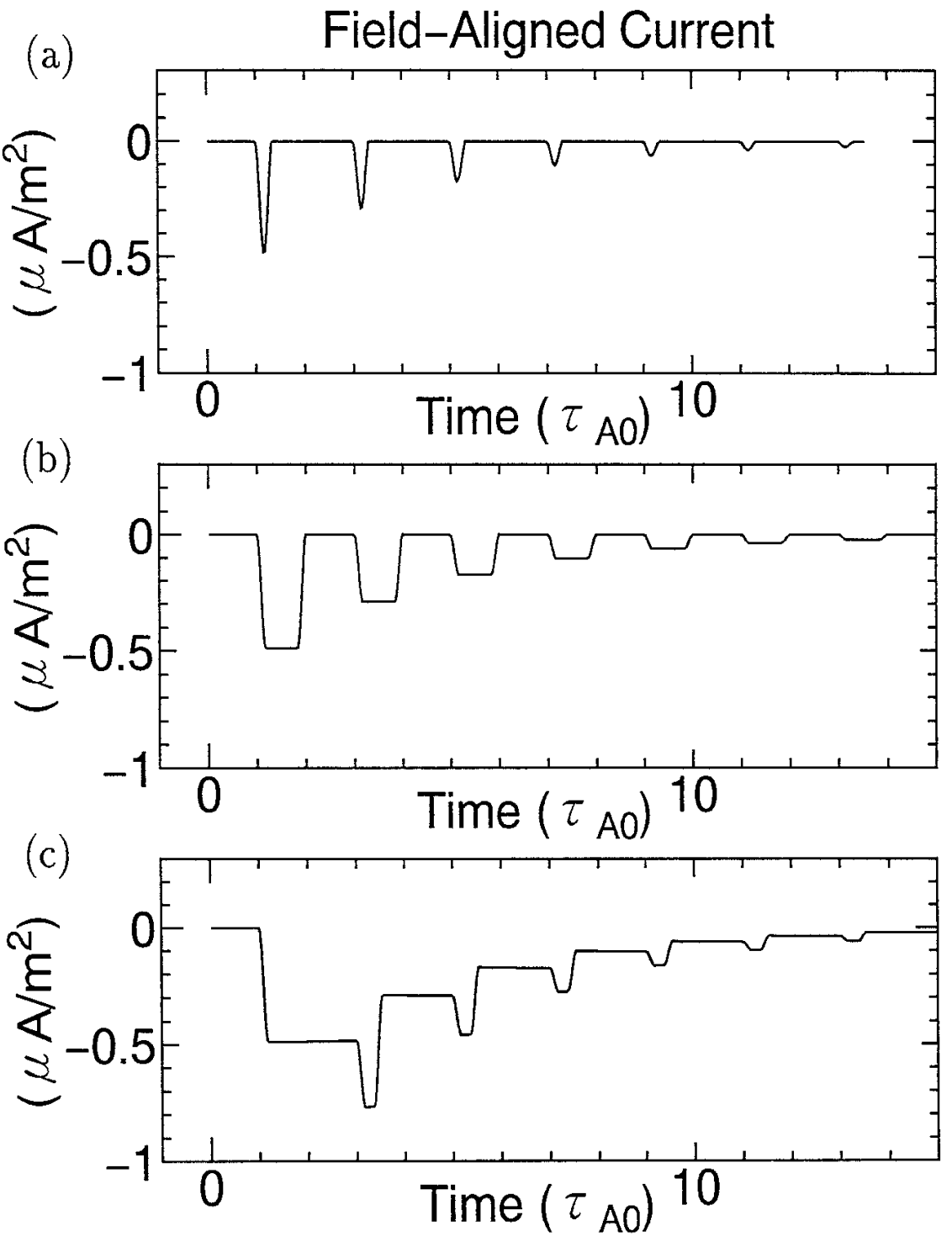

Fig. 6

(a) Electrostatic Potential

(b) Field-Aligned Current

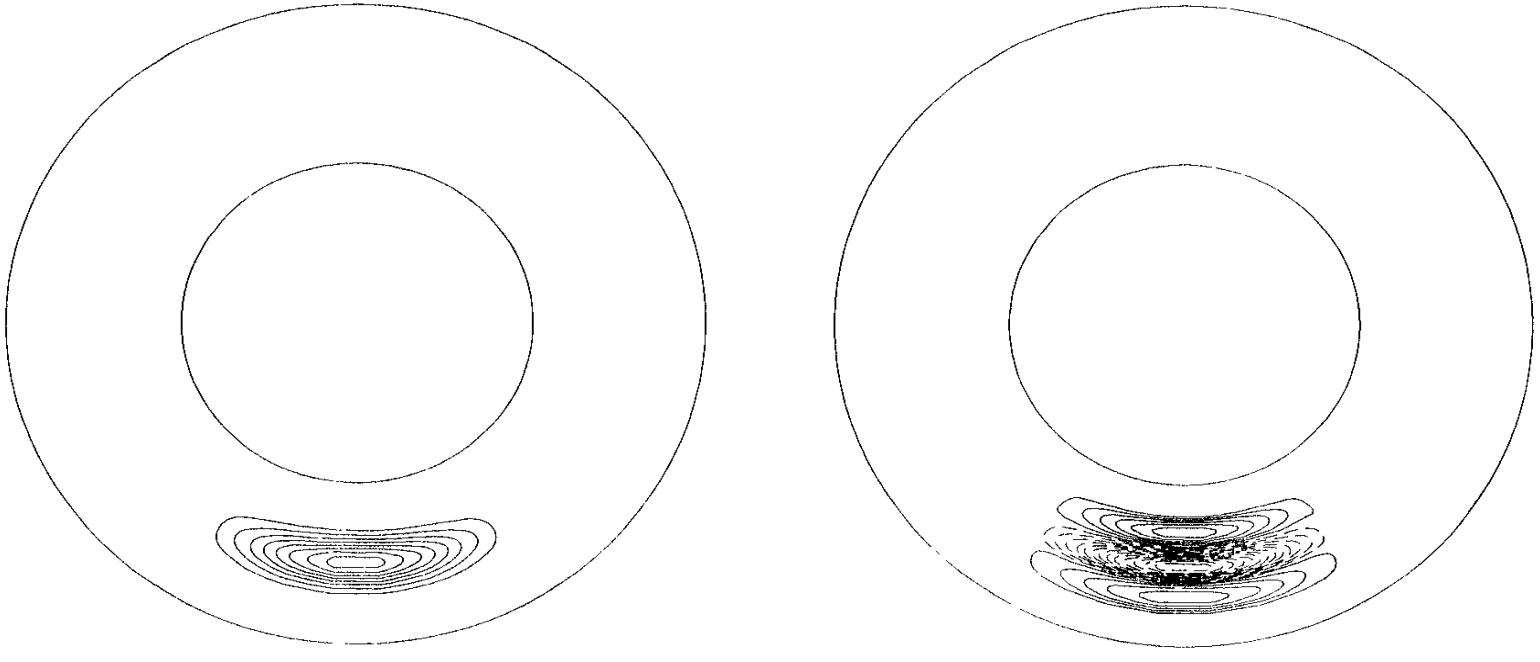

Fig. 7

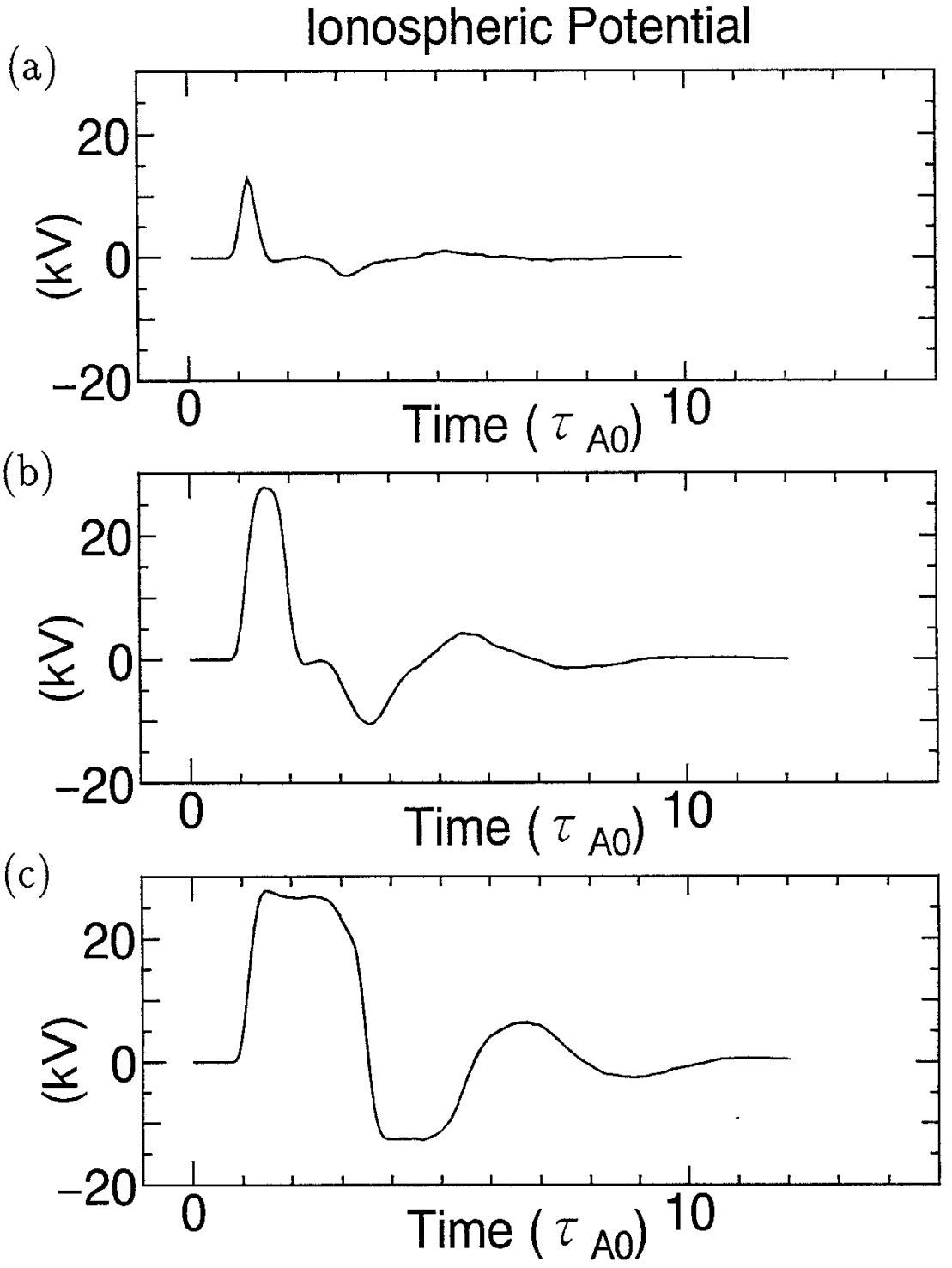
Ionospheric Potential
(a)
20
0
-20
(kV)
0
Time (τ_{A0}) 10
(b)
20
0
-20
(kV)
0
Time (τ_{A0}) 10
(c)
20
0
-20
(kV)
0
Time (τ_{A0}) 10

Fig. 8

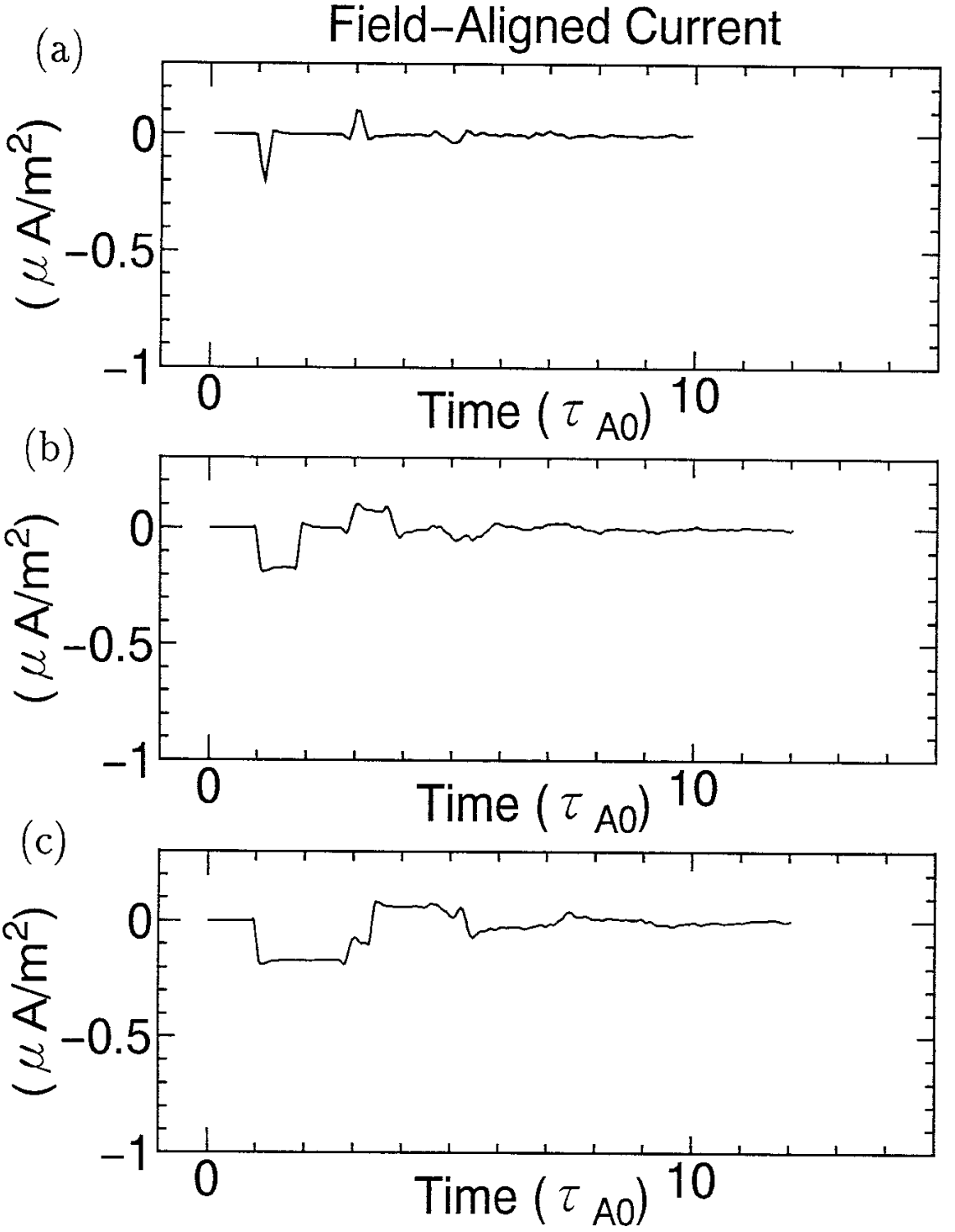

Fig. 9

(a) Electrostatic Potential

(b) Field-Aligned Current

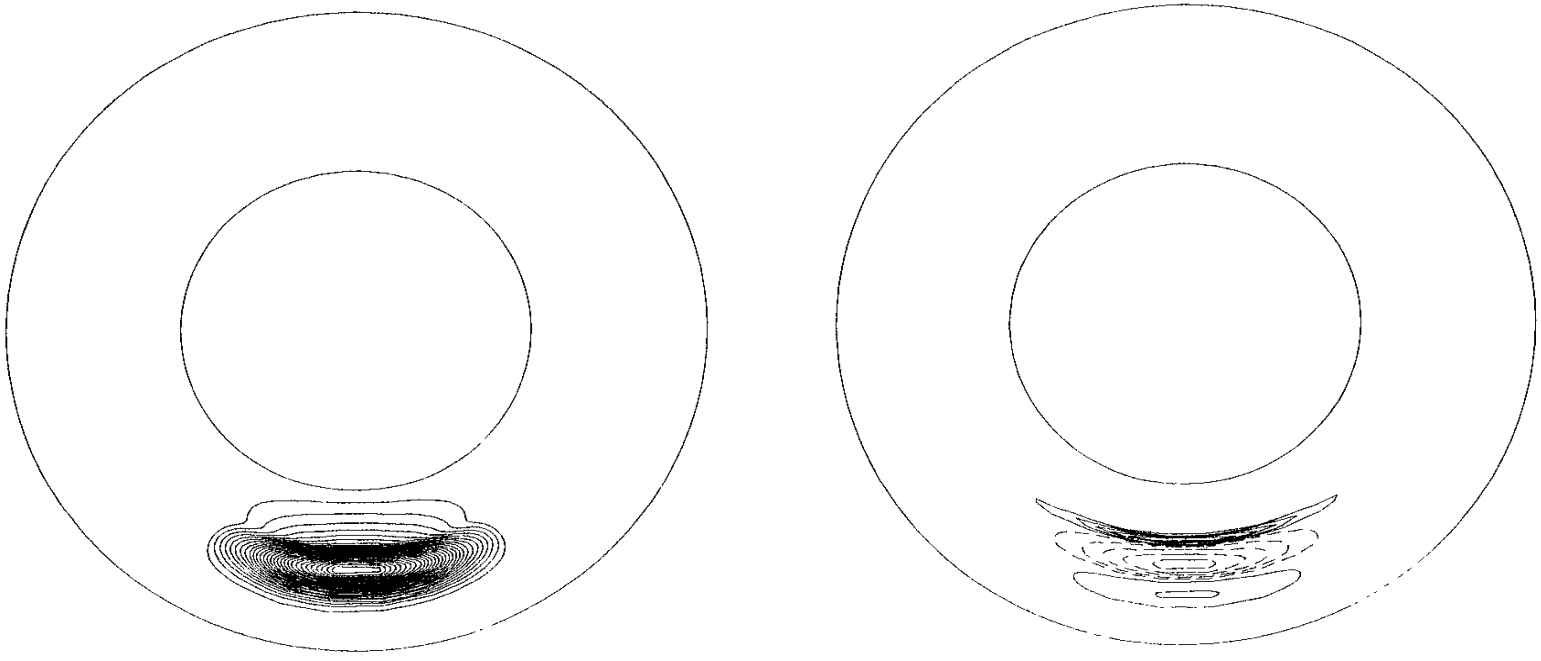

Fig. 10

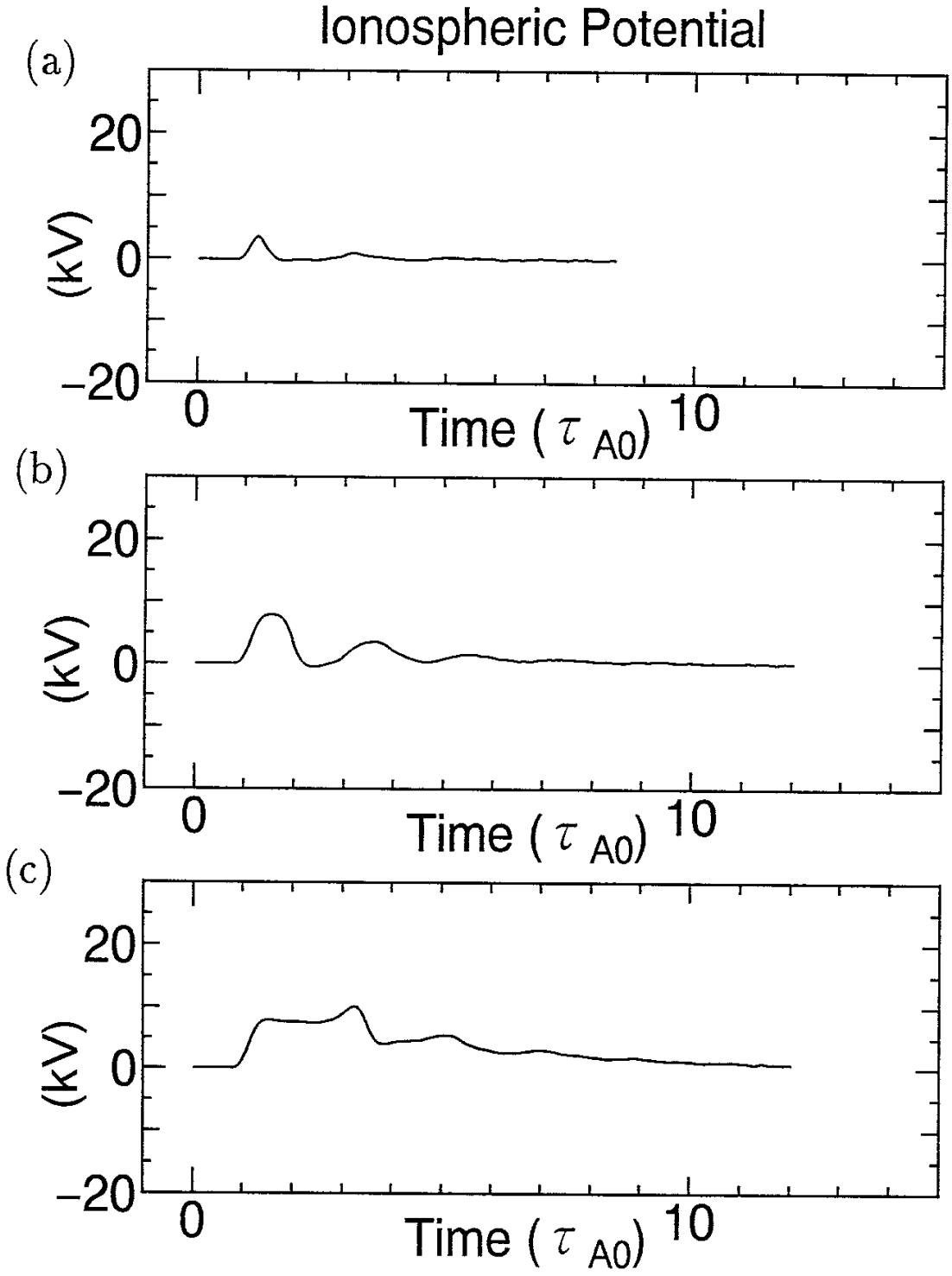
Ionospheric Potential
(a)
20
0
-20
(kV)
0
Time (τ_{A0}) 10
(b)
20
0
-20
(kV)
0
Time (τ_{A0}) 10
(c)
20
0
-20
(kV)
0
Time (τ_{A0}) 10

Fig. 11

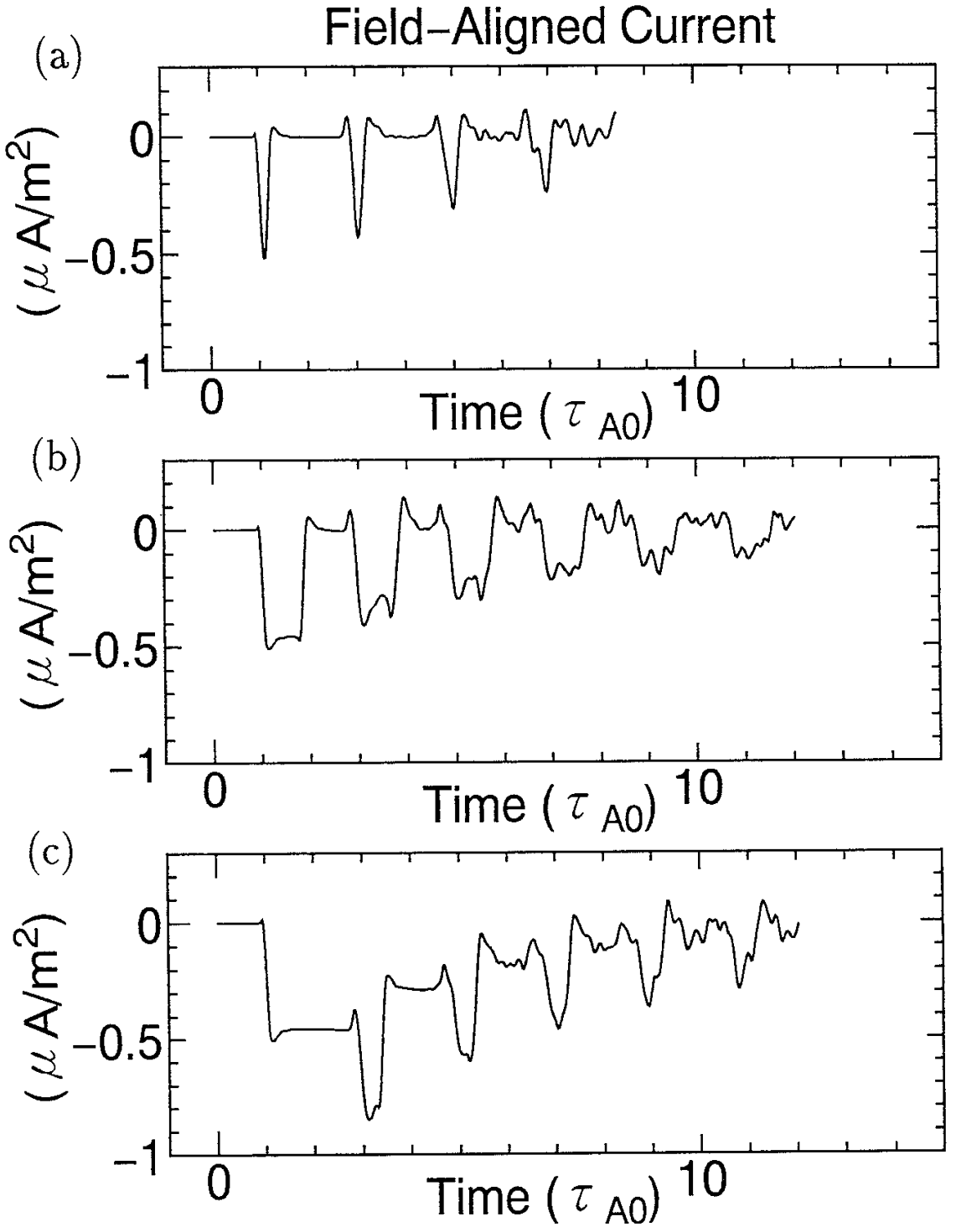

Fig. 12

(a) Electrostatic Potential

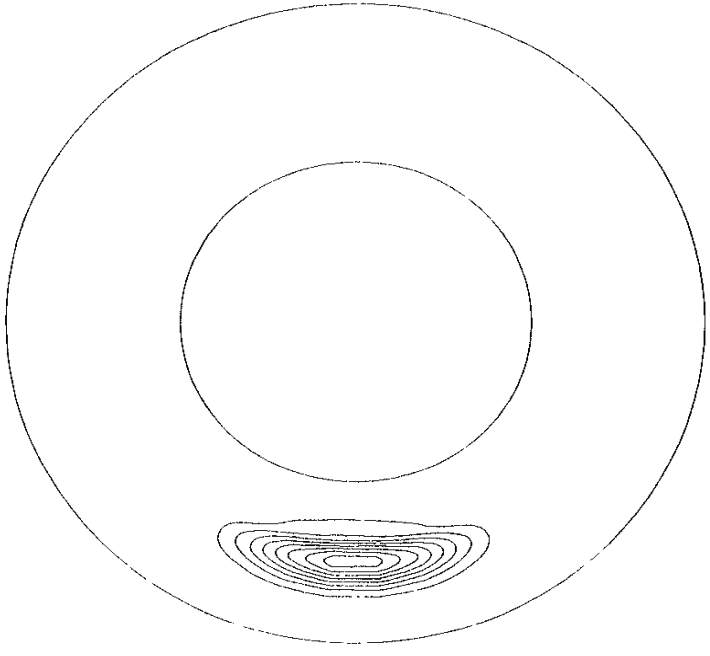

(b) Field-Aligned Current

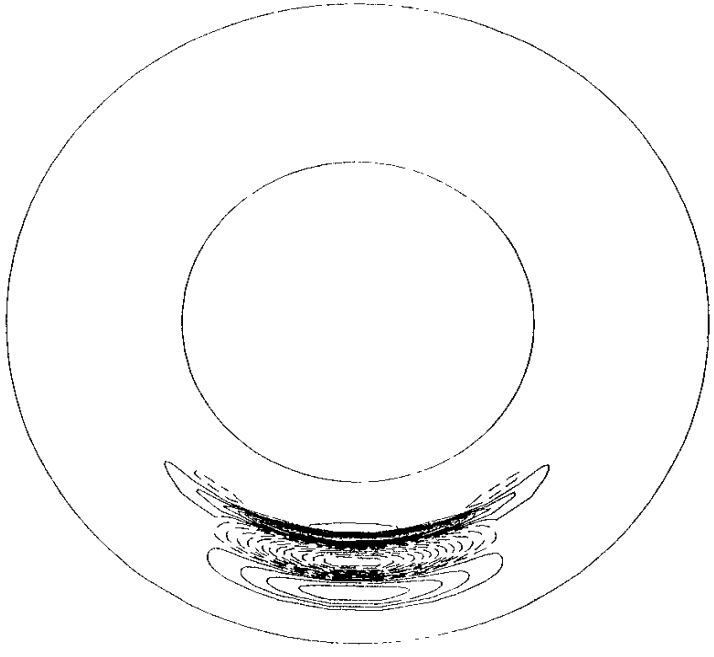

Fig. 13

Recent Issues of NIFS Series

NIFS-229 K. Itoh, M. Yagi, A. Fukuyama, S.-I. Itoh and M. Azumi, *Comment on 'A Mean Field Ohm's Law for Collisionless Plasmas;* June 1993

NIFS-230 H. Idei, K. Ida, H. Sanuki, H. Yamada, H. Iguchi, S. Kubo, R. Akiyama, H. Arimoto, M. Fujiwara, M. Hosokawa, K. Matsuoka, S. Morita, K. Nishimura, K. Ohkubo, S. Okamura, S. Sakakibara, C. Takahashi, Y. Takita, K. Tsumori and I. Yamada, *Transition of Radial Electric Field by Electron Cyclotron Heating in Stellarator Plasmas;* June 1993

NIFS-231 H.J. Gardner and K. Ichiguchi, *Free-Boundary Equilibrium Studies for the Large Helical Device,* June 1993

NIFS-232 K. Itoh, S.-I. Itoh, A. Fukuyama, H. Sanuki and M. Yagi, *Confinement Improvement in H-Mode-Like Plasmas in Helical Systems,* June 1993

NIFS-233 R. Horiuchi and T. Sato, *Collisionless Driven Magnetic Reconnection,* June 1993

NIFS-234 K. Itoh, S.-I. Itoh, A. Fukuyama, M. Yagi and M. *Azumi, Prandtl Number of Toroidal Plasmas;* June 1993

NIFS-235 S. Kawata, S. Kato and S. Kiyokawa , *Screening Constants for Plasma;* June 1993

NIFS-236 A. Fujisawa and Y. Hamada, *Theoretical Study of Cylindrical Energy Analyzers for MeV Range Heavy Ion Beam Probes;* July 1993

NIFS-237 N. Ohyabu, A. Sagara, T. Ono, T. Kawamura and O. Motojima, *Carbon Sheet Pumping;* July 1993

NIFS-238 K. Watanabe, T. Sato and Y. Nakayama, *Q-profile Flattening due to Nonlinear Development of Resistive Kink Mode and Ensuing Fast Crash in Sawtooth Oscillations;* July 1993

NIFS-239 N. Ohyabu, T. Watanabe, Hantao Ji, H. Akao, T. Ono, T. Kawamura, K. Yamazaki, K. Akaishi, N. Inoue, A. Komori, Y. Kubota, N. Noda, A. Sagara, H. Suzuki, O. Motojima, M. Fujiwara, A. Iiyoshi, *LHD Helical Divertor;* July 1993

NIFS-240 Y. Miura, F. Okano, N. Suzuki, M. Mori, K. Hoshino, H. Maeda, T. Takizuka, JFT-2M Group, K. Itoh and S.-I. Itoh, *Ion Heat Pulse after Sawtooth Crash in the JFT-2M Tokamak;* Aug. 1993

NIFS-241 K. Ida, Y.Miura, T. Matsuda, K. Itoh and JFT-2M Group, *Observation of non Diffusive Term of Toroidal Momentum Transport in the JFT-*

2M Tokamak; Aug. 1993

NIFS-242 O.J.W.F. Kardaun, S.-I. Itoh, K. Itoh and J.W.P.F. Kardaun,
Discriminant Analysis to Predict the Occurrence of ELMS in H-Mode Discharges; Aug. 1993

NIFS-243 K. Itoh, S.-I. Itoh, A. Fukuyama,
Modelling of Transport Phenomena; Sep. 1993

NIFS-244 J. Todoroki,
Averaged Resistive MHD Equations; Sep. 1993

NIFS-245 M. Tanaka,
The Origin of Collisionless Dissipation in Magnetic Reconnection; Sep. 1993

NIFS-246 M. Yagi, K. Itoh, S.-I. Itoh, A. Fukuyama and M. Azumi,
Current Diffusive Ballooning Mode in Seecond Stability Region of Tokamaks; Sep. 1993

NIFS-247 T. Yamagishi,
Trapped Electron Instabilities due to Electron Temperature Gradient and Anomalous Transport; Oct. 1993

NIFS-248 Y. Kondoh,
Attractors of Dissipative Structure in Three Disspative Fluids; Oct. 1993

NIFS-249 S. Murakami, M. Okamoto, N. Nakajima, M. Ohnishi, H. Okada,
Monte Carlo Simulation Study of the ICRF Minority Heating in the Large Helical Device; Oct. 1993

NIFS-250 A. Iiyoshi, H. Momota, O. Motojima, M. Okamoto, S. Sudo, Y. Tomita, S. Yamaguchi, M. Ohnishi, M. Onozuka, C. Uenosono,
Innovative Energy Production in Fusion Reactors; Oct. 1993

NIFS-251 H. Momota, O. Motojima, M. Okamoto, S. Sudo, Y. Tomita, S. Yamaguchi, A. Iiyoshi, M. Onozuka, M. Ohnishi, C. Uenosono,
Characteristics of D-^{3}He Fueled FRC Reactor: ARTEMIS-L, Nov. 1993

NIFS-252 Y. Tomita, L.Y. Shu, H. Momota,
Direct Energy Conversion System for D-^{3}He Fusion, Nov. 1993

NIFS-253 S. Sudo, Y. Tomita, S. Yamaguchi, A. Iiyoshi, H. Momota, O. Motojima, M. Okamoto, M. Ohnishi, M. Onozuka, C. Uenosono,
Hydrogen Production in Fusion Reactors, Nov. 1993

NIFS-254 S. Yamaguchi, A. Iiyoshi, O. Motojima, M. Okamoto, S. Sudo,

M. Ohnishi, M. Onozuka, C. Uenosono,
Direct Energy Conversion of Radiation Energy in Fusion Reactor,
Nov. 1993

NIFS-255 S. Sudo, M. Kanno, H. Kaneko, S. Saka, T. Shirai, T. Baba,
Proposed High Speed Pellet Injection System "HIPEL" for Large Helical Device
Nov. 1993

NIFS-256 S. Yamada, H. Chikaraishi, S. Tanahashi, T. Mito, K. Takahata, N. Yanagi, M. Sakamoto, A. Nishimura, O. Motojima, J. Yamamoto, Y. Yonenaga, R. Watanabe,
Improvement of a High Current DC Power Supply System for Testing the Large Scaled Superconducting Cables and Magnets; Nov. 1993

NIFS-257 S. Sasaki, Y. Uesugi, S. Takamura, H. Sanuki, K. Kadota,
Temporal Behavior of the Electron Density Profile During Limiter Biasing in the HYBTOK-II Tokamak; Nov. 1993

NIFS-258 K. Yamazaki, H. Kaneko, S. Yamaguchi, K.Y. Watanabe, Y.Taniguchi, O.Motojima, LHD Group,
Design of Central Control System for Large Helical Device (LHD); Nov. 1993

NIFS-259 K. Yamazaki, H. Kaneko, S. Yamaguchi, K.Y. Watanabe, Y.Taniguchi, O.Motojima, LHD Group,
Design of Central Control System for Large Helical Device (LHD); Nov. 1993

NIFS-260 B.V.Kuteev,
Pellet Ablation in Large Helical Device; Nov. 1993

NIFS-261 K. Yamazaki,
Proposal of "MODULAR HELIOTRON': Advanced Modular Helical System Compatible with Closed Helical Divertor; Nov. 1993

NIFS-262 V.D.Pustovitov,
Some Theoretical Problems of Magnetic Diagnostics in Tokamaks and Stellarators; Dec. 1993

NIFS-263 A. Fujisawa, H. Iguchi, Y. Hamada
A Study of Non-Ideal Focus Properties of 30 ° Parallel Plate Energy Analyzers; Dec. 1993

NIFS-264 K. Masai,
Nonequilibria in Thermal Emission from Supernova Remnants; Dec. 1993

NIFS-265 K. Masai, K. Nomoto,

X-Ray Enhancement of SN 1987A Due to Interaction with its Ring-like Nebula; Dec. 1993

NIFS-266 J. Uramoto
A Research of Possibility for Negative Muon Production by a Low Energy Electron Beam Accompanying Ion Beam; Dec. 1993

NIFS-267 H. Iguchi, K. Ida, H. Yamada, K. Itoh, S.-I. Itoh, K. Matsuoka, S. Okamura, H. Sanuki, I. Yamada, H. Takenaga, K. Uchino, K. Muraoka,
The Effect of Magnetic Field Configuration on Particle Pinch Velocity in Compact Helical System (CHS); Jan. 1993

NIFS-268 T. Shikama, C. Namba, M. Kosuda, Y. Maeda,
Development of High Time-Resolution Laser Flash Equipment for Thermal Diffusivity Measurements Usting Miniature-Size Specimens; Jan. 1994

NIFS-269 T. Hayashi, T. Sato, P. Merkel, J. Nührenberg, U. Schwenn,
Formation and 'Self-Healing' of Magnetic Islands in Finite-β Helias Equilibria; Jan. 1994

NIFS-270 S. Murakami, M. Okamoto, N. Nakajima, T. Mutoh,
Efficiencies of the ICRF Minority Heating in the CHS and LHD Plasmas; Jan. 1994

NIFS-271 Y. Nejoh, H. Sanuki,
Large Amplitude Langmuir and Ion-Acoustic Waves in a Relativistic Two-Fluid Plasma; Feb. 1994

NIFS-272 A. Fujisawa, H. Iguchi, A. Taniike, M. Sasao, Y. Hamada,
A 6MeV Heavy Ion Beam Probe for the Large Helical Device; Feb. 1994

NIFS-273 Y. Hamada, A. Nishizawa, Y. Kawasumi, K. Narihara, K. Sato, T. Seki, K. Toi, H. Iguchi, A. Fujisawa, K. Adachi, A. Ejiri, S. Hidekuma, S. Hirokura, K. Ida, J. Koong, K. Kawahata, M. Kojima, R. Kumazawa, H. Kuramoto, R. Liang, H. Sakakita, M. Sasao, K. N. Sato, T. Tsuzuki, J. Xu, I. Yamada, T. Watari, I. Negi,
Measurement of Profiles of the Space Potential in JIPP T-IIU Tokamak Plasmas by Slow Poloidal and Fast Toroidal Sweeps of a Heavy Ion Beam; Feb. 1994

NIFS-274 M. Tanaka,
A Mechanism of Collisionless Magnetic Reconnection; Mar. 1994

NIFS-275 A. Fukuyama, K. Itoh, S.-I. Itoh, M. Yagi and M. Azumi,
Isotope Effect on Confinement in DT Plasmas; Mar. 1994